

OCEANOGRAPHY

Unprecedented reduction and quick recovery of the South Indian Ocean heat content and sea level in 2014–2018

Denis L. Volkov^{1,2*}, Sang-Ki Lee², Arnold L. Gordon³, Michael Rudko^{1,2}

Following the onset of the strong 2014–2016 El Niño, a decade-long increase of the basin-wide sea level and heat content in the subtropical southern Indian Ocean (SIO) in 2004–2013 ended with an unprecedented drop, which quickly recovered during the weak 2017–2018 La Niña. Here, we show that the 2014–2016 El Niño contributed to the observed cooling through an unusual combination of both the reduced heat advection from the Pacific (dominant in the eastern SIO) and the basin-wide cyclonic wind anomaly that led to shoaling of isotherms (dominant in the western SIO). The ensuing recovery was mainly forced by an anticyclonic wind anomaly associated with stronger trade winds that caused deepening of isotherms and upper-ocean warming, effectively suppressing the 2014–2016 cooling signal propagating from the eastern boundary. The results presented here highlight the complexity of the SIO heat content variability driven by remote and local forcing.

INTRODUCTION

The ocean absorbs about 93% of the excess heat, accumulated in the Earth's climate system due to the net radiation imbalance at the top of the atmosphere (1). The subtropical southern Indian Ocean (SIO) has been characterized as one of the major heat accumulators among the oceanic basins due to its remarkable warming during the past two decades (2–4). Heat advection from the Pacific into the SIO has been identified as the dominant mechanism for the slowdown of the global mean surface warming during the first decade of the 21st century (5). The accumulation of heat has led to an accelerated regional sea level rise (6), intensifications of tropical cyclones (7) and Indian summer monsoon rainfall (8), more frequent and long-lasting marine heat waves (9), and coral bleaching events (10).

The interannual-to-decadal variability of heat content and sea level in the SIO is strongly influenced by its connection with the Pacific and large-scale climatic forcing in the Indo-Pacific region primarily associated with El Niño–Southern Oscillation (ENSO), Indian Ocean Dipole (IOD), and Southern Annular Mode (SAM) (11). The remote ENSO effect on the SIO heat content is twofold. First, ENSO drives changes in the upper-ocean heat content in the western equatorial Pacific and, therefore, modulates advection into the SIO from the Pacific (4, 5, 12), which we term here the “ocean tunnel” effect. Second, local changes in wind stress curl influencing the upper-ocean heat content in the SIO are also related to ENSO by the means of atmospheric teleconnections via the Walker Circulation (11), which we call here the “atmospheric bridge” effect. While the atmospheric bridge is a rather fast teleconnection, it takes years for the ocean tunnel signals to reach the western Indian Ocean. The IOD events are often triggered by ENSO. However, they are not always in-phase with ENSO because about one-third of IOD events occur independently of ENSO events, subject to tropical preconditioning in the eastern Indian Ocean (13–15).

The main conduit of warm water from the Pacific to the SIO is the Indonesian Throughflow (ITF), with a mean transport of about 15 Sverdrups ($1 \text{ Sv} = 10^6 \text{ m}^3 \text{ s}^{-1}$) (16). The ITF is driven by the Indo-Pacific interocean pressure gradient set up by trade winds in the Pacific and equatorial winds in the (mainly eastern) Indian Ocean (17–20). By maintaining interocean exchanges, the ITF and the system of currents in the SIO (Fig. 1) are important components of the global meridional overturning circulation (21). The major part of the ITF water is carried westward by the South Equatorial Current (SEC) and eventually enters the Atlantic Ocean via the Agulhas leakage and rings (22–24). Near the eastern boundary of the SIO, part of the ITF waters also makes its way to the southward-flowing Leeuwin Current (LC) off the west Australian coast (25). The ITF is generally stronger during La Niña conditions and positive IOD events, and it is weaker during El Niño conditions and negative IOD events (26–33).

Besides the advection by the SEC and LC, temperature anomalies originated in the Pacific and entering the SIO via the ITF can affect coastally trapped waves along the west Australian coast, which are often produced by equatorial Kelvin waves (Fig. 1) (34–37). In the southeast tropical Indian Ocean, these signals can radiate westward from the eastern boundary as Rossby waves and eventually affect sea level and heat content in the SIO interior and near the western boundary (38, 39). In addition, instabilities of the LC generate meso-scale eddies that propagate westward and contribute to the transfer of heat toward the SIO interior (39). On seasonal-to-interannual time scales, local wind forcing, through Ekman pumping over the open ocean and coastal upwelling, is also able to generate Rossby waves and/or modify those emanated from the eastern boundary (40, 41).

The La Niña-like conditions that persisted in the Pacific in 2005–2013, as shown by the Multivariate ENSO Index (MEI), ended rather abruptly with the 2014–2016 El Niño, which happened to be nearly as strong as the strongest on record 1997–1998 El Niño event (Fig. 2A). The superposition of the 2014–2016 El Niño and the lowest on record negative IOD event in 2016 (Fig. 2A) led up to 40% decrease of the ITF volume and heat transports (12, 33, 42). As evidenced by satellite altimetry measurements and the thermosteric sea level component derived from Argo temperature data, the

Copyright © 2020
The Authors, some
rights reserved;
exclusive licensee
American Association
for the Advancement
of Science. No claim to
original U.S. Government
Works. Distributed
under a Creative
Commons Attribution
NonCommercial
License 4.0 (CC BY-NC).

¹Cooperative Institute for Marine and Atmospheric Studies, University of Miami, Miami, FL 33149, USA. ²National Oceanic and Atmospheric Administration, Atlantic Oceanographic and Meteorological Laboratory, Miami, FL 33149, USA. ³Lamont-Doherty Earth Observatory, Columbia University, Palisades, NY 10964, USA.

*Corresponding author. Email: denis.volkov@noaa.gov

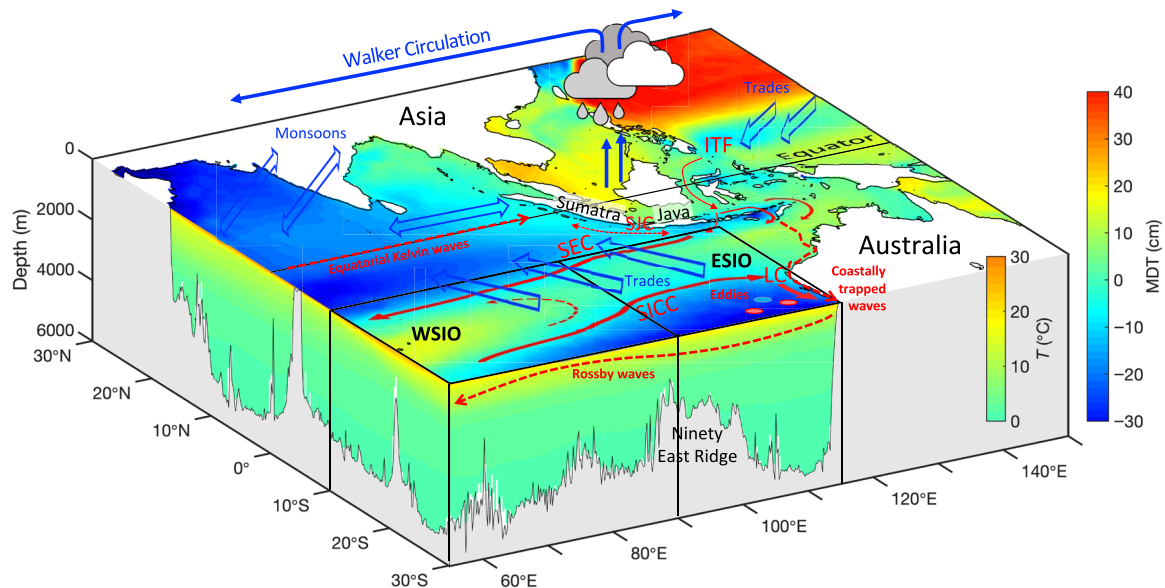


Fig. 1. Schematic showing the dynamic processes affecting the subtropical SIO heat content and sea level. Color shows the mean dynamic topography (MDT) in the horizontal plane and temperature climatology in the vertical planes. The atmospheric circulation in the SIO is dominated by southeasterly trade winds. The general ocean circulation consists of the Indonesian Throughflow (ITF) that feeds the South Equatorial Current (SEC) and the Leeuwin Current (LC), and the South Indian Counter Current (SICC). ENSO affects the SIO heat content via the ocean route (ITF) and atmospheric route (atmospheric bridge due to Walker Circulation). The ITF volume and heat transports into the eastern SIO (ESIO) increase during La Niña conditions (stronger trade winds in the Pacific) and decrease during El Niño conditions (weaker trade winds in the Pacific). Besides advection, signals generated in the Pacific reach the coast of West Australia as coastally trapped waves. Then, these signals propagate toward the western SIO (WSIO) as eddies and Rossby waves. Local wind stress curl can modify the waves radiated from the eastern boundary and/or generate other waves.

decade-long accumulation of the upper 2000-m heat content in the SIO subtropical gyre in 2004–2013 also ended with an unprecedented (in observational record) cooling in 2014–2016 (Fig. 2A). However, heat content in the SIO nearly recovered during the next 2 years, following a switch from the strong 2014–2016 El Niño to the weak 2017–2018 La Niña. Such a rapid response is compelling and, as will be shown below, cannot be accounted for by the westward propagation of warming anomalies originated in the Pacific. What is also puzzling is that the response of sea level (and presumably heat content) averaged over the SIO subtropical gyre to the strongest on record 1997–1998 El Niño was much weaker than that to the recent 2014–2016 El Niño (Fig. 2A).

The main objective of this study is to investigate the fate of the unprecedented 2014–2016 cooling in the SIO subtropical gyre and to elucidate the mechanisms responsible for this cooling and for the subsequent recovery in 2017–2018. Prior periods back to the advent of high-accuracy satellite altimetry in 1993 are also considered, with a particular objective to characterize the difference in oceanic and atmospheric conditions during the two strongest on record El Niño events in 1997–1998 and in 2014–2016.

RESULTS

Observed sea level and heat content changes

On the basis of satellite altimetry and Argo data, sea level and heat content, expressed as the thermobaric sea level component, in the SIO subtropical gyre were increasing in 2004–2013 (Fig. 2, A and B) associated with La Niña-like conditions in the Pacific and driven by an increased ITF transport (4). The gyre-scale release of the accumulated heat followed the onset of the very strong 2014–2016 El Niño

and brought the heat content values below the levels observed at the beginning of Argo era in 2004 (Fig. 2A). Consistent with this change, satellite altimetry data show the gyre-scale reduction of sea-level anomaly (SLA) from 2014 to 2016 (Fig. 2, C and D).

Geostrophy implies that the SEC, situated over the latitude band of about 10° to 20°S, was stronger than the average in 2014 (Fig. 2C) and became substantially weaker in 2016 (Fig. 2D). This is expected, because the ITF, which contributes to the SEC transport, also decreased in 2014–2016 (33, 42). In addition, westerly equatorial wind anomalies led to a negative IOD event in 2016 (blue curve in Fig. 2A), associated with a deepening of the thermocline and higher sea levels to the west and south of Sumatra and Java (Fig. 2D), and thus contributed to the reduction of the ITF transport (43).

Heat content in the SIO subtropical gyre quickly recovered in 2017–2018 following a switch from the 2014–2016 El Niño to the weak 2017–2018 La Niña (Fig. 2A). Satellite altimetry data in 2018 suggest that heat content recovery was not associated with a gyre-wide increase of SLA (Fig. 2E). Instead, sea level increased in the western SIO (WSIO; west of the Ninety East Ridge), while the eastern SIO (ESIO; east of the Ninety East Ridge) still exhibited low SLA remaining there since the 2014–2016 El Niño. This observation raises a question on whether the weak La Niña in 2017–2018 and the westward propagation of associated temperature anomalies from the eastern boundary had any notable contribution to the heat content variability in the WSIO in 2014–2018.

A longitude-time diagram of SLA averaged between 10°S and 30°S and stretching from the eastern boundary at 115°E to 55°E (Fig. 3A) shows that the westward propagation of interannual SLA signals has been the most prominent feature over the entire satellite altimetry record since 1993. However, one can note that some signals

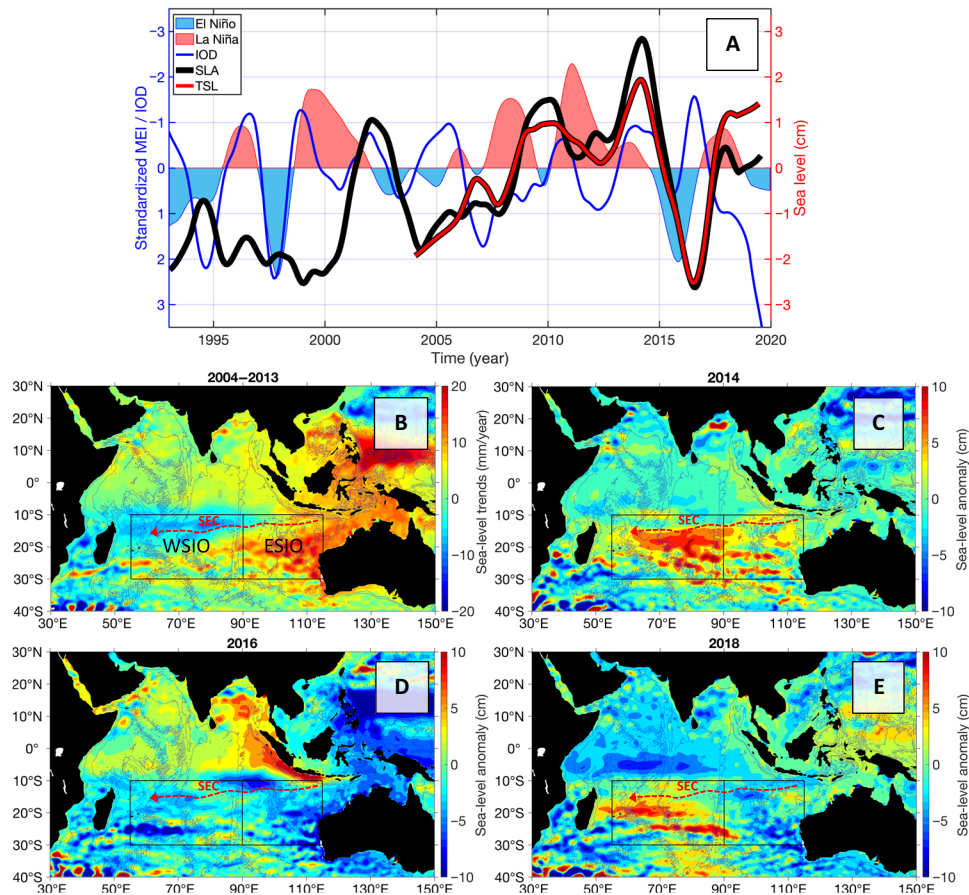


Fig. 2. Sea level changes, ENSO, and IOD. (A) Time series of (color shading) the standardized (divided by standard deviation, SD) MEI (El Niño/La Niña conditions are shown by blue/pink shading) and (blue curve) IOD index; (black curve) sea-level anomaly (SLA) from altimetry, and (red curve) thermosteric SLA from Argo data averaged over 55°E to 115°E and 10°S to 30°S. The time series are low-pass filtered with a cutoff period of 1 year. (B) Dynamic sea-level trends in 2004–2013 (global mean sea level is subtracted). During this time, the SIO was characterized as one of the major heat accumulators among the oceanic basins. (C to E) SLA relative to the record mean value and averaged in 2014, 2016, and 2018, respectively. The approximate location of the SEC is shown by red dashed arrows. Blue contours show the bottom topography for 2000, 4000, and 6000 m.

observed at the eastern boundary were able to reach the western boundary, while others were disturbed by local processes and hardly able to cross the Ninety East Ridge. For example, two positive SLA at the eastern boundary, associated with La Niña conditions in 1999–2001 and 2010–2013, propagated westward and reached 55°E about 2 to 3 years later. The amplitude of the 1999–2001 anomaly substantially decreased to the west of the Ninety East Ridge. The strongest on record 1997–1998 El Niño event generated a negative SLA at the eastern boundary, which was amplified to the west of the Ninety East Ridge and reached the western boundary around 2000. Among those SLA signals that did not propagate far beyond the Ninety East Ridge are the 2003–2007 and 2015–2016 negative anomalies.

Displayed in Fig. 3 (B and C) are the time series of SLA from altimetry, and the steric, thermosteric, and halosteric SLAs computed from Argo data, averaged over the WSIO (55°E to 90°E and 10°S to 30°S; Fig. 3B) and over the ESIO (90°E to 115°E and 10°S to 30°S; Fig. 3C). The variability of sea level in both regions is mostly steric. Although the halosteric component has an amplitude of about 1 cm and, thus, makes a sizable contribution to the variability, the thermosteric component is dominant. This suggests that SLA from altimetry is a good indicator of heat content changes in the entire SIO subtropical gyre. The variability of SLA in the WSIO and ESIO is quite different, although the westward propagation can be easily traced in

many cases (compare to Fig. 3A). The SLA signals that radiate westward from the eastern boundary are strongly linked to ENSO (Fig. 3C). This suggests that their origin is very likely related to the ocean tunnel effect, i.e., the ITF and coastally trapped waves that rapidly transfer anomalies generated in the Pacific along the west Australian coast.

A positive SLA observed at the eastern boundary during the 1996 La Niña reached the WSIO in 1997–1998. A negative SLA observed in the ESIO during the 1997–1998 El Niño reached the WSIO in 1999–2000, at the time when a strong positive SLA associated with the 1999–2001 La Niña was already present at the eastern boundary. Note that in 1998, an in-phase SLA response to 1997–1998 El Niño in the ESIO was compensated for by a delayed SLA response to the 1996 La Niña in the WSIO (Fig. 3). Therefore, although ENSO signals in 1996–1998 did influence the regional SLA via the ocean tunnel effect, the net basin-wide change of SLA during this time was small (Fig. 2A). The 1999–2001 La Niña signal (positive SLA at the eastern boundary) reached the WSIO in 2002–2003. Relatively high SLA persisted in the WSIO until 2010, while strong negative SLA was present in the ESIO in 2003–2006 and barely propagated west of the Ninety East Ridge (Fig. 3).

A negative SLA in the WSIO in 2011–2013 was notably stronger and more robust than a weak transient 2010 anomaly in the ESIO (east of 110°E; Fig. 3A), which suggests that it was largely generated

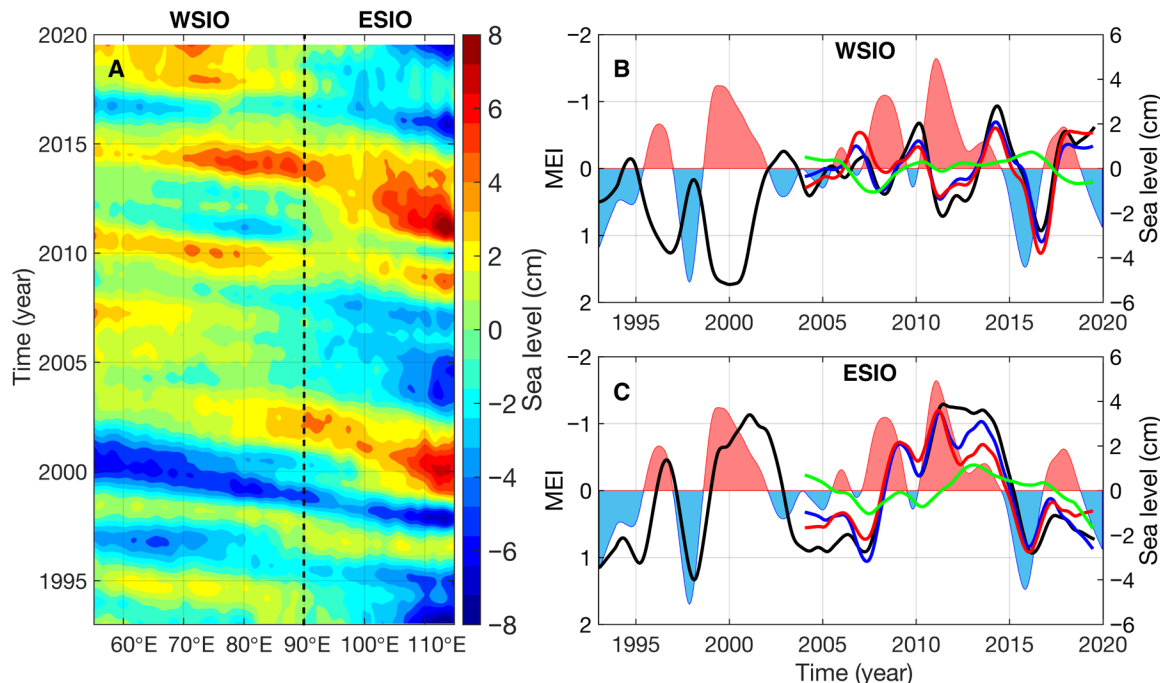


Fig. 3. Sea-level variability and Rossby waves. (A) Hovmöller (longitude-time) diagram of the low-pass-filtered SLA with a cutoff period of 1 year averaged between 10°S and 30°S. (B and C) Low-pass-filtered MEI (shaded area) and sea level components averaged over (B) 55°E to 90°E and 10°S to 30°S (WSIO) and over (C) 90°E to 115°E and 10°S to 30°S (ESIO). The sea level components include (black) SLA from satellite altimetry and (blue, red, green) steric (SSL), thermosteric (TSL), and halosteric (HSL) SLAs, respectively, computed from Argo data.

by local processes rather than propagated from the east. Last, although a strong negative SLA at the eastern boundary in 2015–2016 was likely associated with an SLA minimum in the WSIO in 2016 (Fig. 3, B and C), its westward propagation can only be traced to about 95°E (Fig. 3A). Consistently, the negative SLA in the WSIO in 2016 occurred almost simultaneously everywhere west of the Ninety East Ridge without any sign of westward propagation. The following increase of SLA in the WSIO in 2016–2019 was apparently caused by local forcing rather than propagated from the ESIO, where negative SLA persisted in 2015–2019. This suggests that local processes can at times be the dominant drivers of sea level and heat content changes in the WSIO. In the following sections, we will explore in more detail what mechanisms can strongly modify or even suppress the ENSO-related signals in the SIO.

Local wind forcing

On annual average, the lower atmospheric circulation over the SIO is dominated by southeasterly trade winds, which are part of the large-scale anticyclonic circulation. The associated positive wind stress curl drives Ekman downwelling (negative Ekman pumping) and leads to downward-doming isotherms centered at around 20°S. Therefore, cyclonic (i.e., clockwise) and anticyclonic (i.e., anticlockwise) wind anomalies in the SIO lead to the upper-ocean cooling and warming, respectively (represented by the blue and red shadings, respectively, in Fig. 4).

The regression of wind and Ekman pumping anomalies on MEI (Fig. 4A) shows that El Niño events (i.e., positive MEI) are associated with weaker trade winds in the SIO and easterly wind anomalies along the equator. This atmospheric circulation pattern favors negative Ekman pumping anomaly in the northeastern SIO and positive

Ekman pumping anomaly in the southwestern SIO, leading to the upper-ocean warming and cooling, respectively. The opposite occurs during La Niña events (i.e., negative MEI). The regression of wind and Ekman pumping anomalies on the IOD index (blue curve in Fig. 2A) shows that easterly equatorial wind anomalies can lead to the upper-ocean warming between about 15°S to 15°N during a positive IOD phase and vice versa during a negative IOD phase, with a rather small response in the subtropical SIO (Fig. 4B).

A comparison of atmospheric circulation patterns during the two strongest El Niño events in 1997–1998 (Fig. 4C) and in 2014–2016 (Fig. 4E) provides another explanation why the basin-wide oceanic response to the former was much weaker than that to the latter. The two main differences between these two time periods were the presence of strong easterly equatorial winds in 1997–1998, which was not observed in 2014–2016, and the presence of basin-wide cyclonic wind anomaly in 2014–2016, which was not found in 1997–1998. It should be noted that the 1997–1998 El Niño happened in phase with a strong positive IOD (Fig. 2A), which led to an amplification of easterly wind anomalies in the tropics (Fig. 4, A and C), inhibiting the formation of a cyclonic wind anomaly in the subtropical SIO. Strong equatorial easterlies in 1997–1998 generated downward Ekman pumping anomalies and favored the upper-ocean warming in the tropics, apparently compensating for the El Niño-generated cooling in the ESIO from the ocean tunnel effect. In 1998–2001, westerly wind anomalies associated with a strong La Niña (Fig. 2A) developed along the equator, and trade winds over the SIO strengthened and shifted westward, leading to the upper-ocean cooling in the northern-northeastern SIO and warming in the southern-southwestern SIO (Fig. 4D).

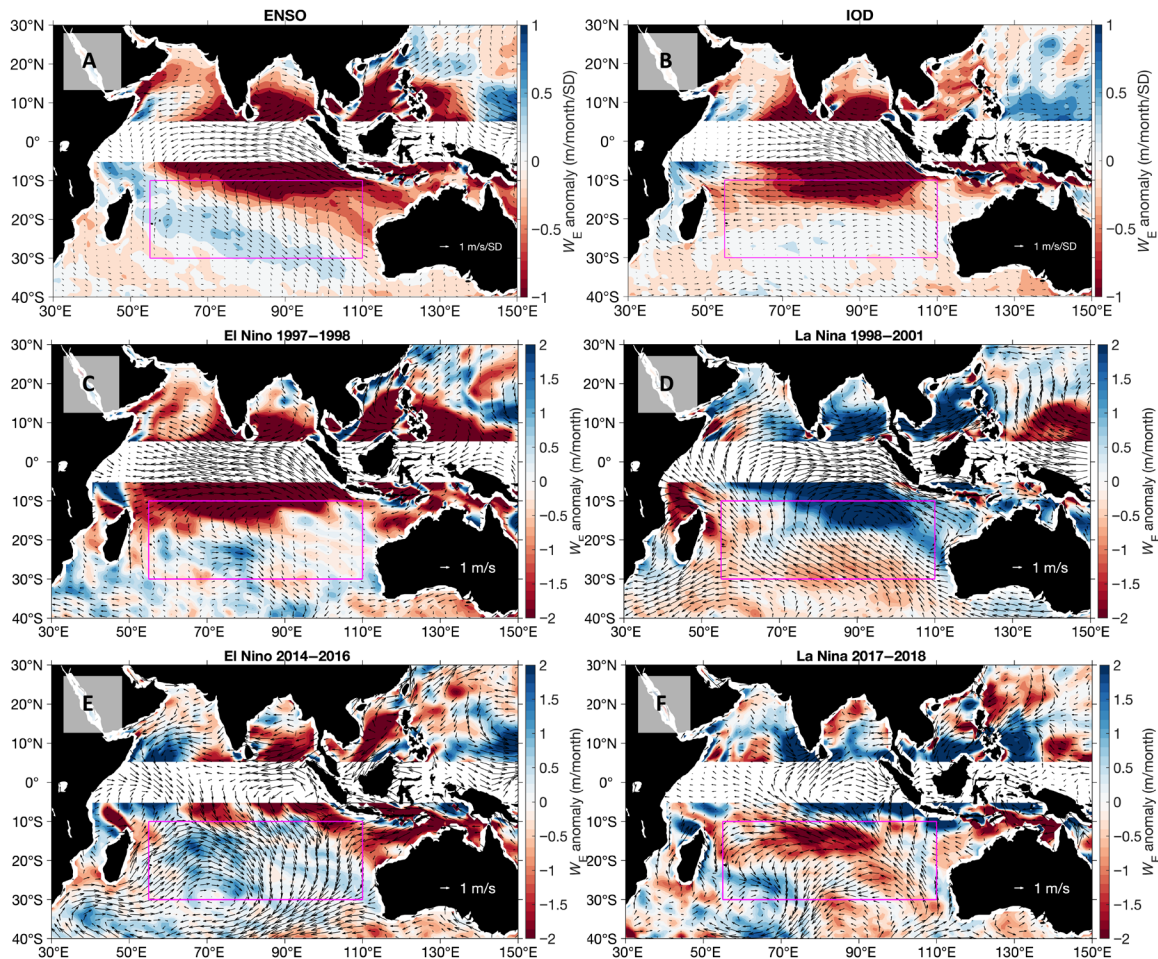


Fig. 4. Wind forcing over the Indian Ocean. (A and B) Regression of Ekman pumping (color shading) and 10-m winds (arrows) on (A) MEI and (B) IOD index, expressed in meter per month per 1 SD change of the respective index. (C to F) Ekman pumping and 10-m wind speed averaged for (C) 1997–1998 El Niño, (D) 1998–2001 La Niña, (E) 2014–2016 El Niño, and (F) 2017–2018 La Niña. Ekman pumping anomalies between 5°S and 5°N are blanked because $f \rightarrow 0$ toward the equator. Negative (positive) Ekman pumping anomalies associated with the upper-ocean warming (cooling) are shown by red (blue) color. Magenta rectangles show the area (55°E to 110°E and 10°S to 30°S) used to plot a longitude-time diagram of Ekman pumping anomaly in fig. S1A.

The 2014–2016 El Niño featured a weak positive IOD in 2015 and the lowest on record negative IOD in 2016 (Fig. 2A). The abrupt release of the accumulated heat in 2014–2016 and the following heat content recovery in 2017–2018 in the SIO align well with wind stress curl anomalies during those periods (Fig. 4, E and F). In contrast to the 1997–1998 El Niño, the 2014–2016 El Niño was characterized by weaker southeasterly trade winds and a cyclonic (clockwise) wind anomaly over the entire SIO (Fig. 4E). This led to Ekman divergence and associated (upward) Ekman pumping anomalies, which favored the observed reduction of the upper-ocean heat content. In 2017–2018, southeasterly trade winds strengthened, leading to downward Ekman pumping anomalies over most of the SIO (Fig. 4F). This change in the surface atmospheric circulation was largely responsible for the observed recovery of heat content in the SIO, which will be qualitatively and quantitatively demonstrated in the remainder of the manuscript.

The observed differences in local wind forcing during the 1997–1998 and 2014–2016 El Niño events challenge the effectiveness of the atmospheric bridge. However, the atmospheric bridge was apparently efficient during the strong La Niña conditions in 1999–2001, 2008,

and 2010–2012, as demonstrated by a longitude-time diagram of Ekman pumping anomalies averaged over 10°S to 30°S with the overlaid time series of MEI and IOD index (fig. S1A). During these time intervals, trade winds strengthened, and cyclonic (clockwise) wind anomalies developed in the ESIO and led to the upward Ekman pumping anomalies and upper-ocean cooling (e.g., Fig. 4D). Statistically significant (at 95% confidence level) negative correlation coefficients between the Ekman pumping anomalies averaged over 10°S to 30°S and MEI are obtained to the east of 95°E (fig. S1B). This indicates that there is wind-driven upper-ocean warming in the ESIO during El Niño, which partly balances respective cooling anomalies advected from the Pacific via the ocean tunnel effect and vice versa during La Niña. Correlation between the Ekman pumping and IOD index is also negative and marginally significant in the ESIO (fig. S1B). This is because the IOD-related equatorial winds directly contribute to Ekman pumping anomalies in the ESIO. More specifically, easterly equatorial winds during a positive IOD phase are associated with downward (negative) Ekman pumping anomalies and vice versa during a negative IOD phase. In the WSIO, neither MEI nor IOD index is significantly correlated with Ekman pumping, suggesting

that none of these climate modes are able to explain the complexity of local wind variability.

Upper-ocean temperature changes

As demonstrated in the previous section, wind stress curl anomalies in 2014–2018 were consistent with a strong reduction of the upper-ocean heat content in 2014–2016 and a quick recovery in 2017–2018. It is instructive to analyze how the upper-ocean temperature structure observed by Argo floats was changing with depth and latitude over these time intervals. Similar to other subtropical ocean basins, the zonally averaged upper-ocean temperature profile in the SIO is characterized by downward-doming isotherms, with a maximum heat content centered at about 20°S (e.g., see Fig. 5, A and B), bounded by the SEC to the north and the South Indian Counter Current (SICC) to the south (Fig. 1). In 2014–2016, the upper 1000 m of the subtropical SIO experienced rather strong cooling south of 10°S, with a maximum temperature reduction of up to 0.8°C observed at about 300-m depth below the Ekman layer (Fig. 5, A and C). At the same time, temperature increased by more than 1°C in the upper 200 m to the north of 10°S. These changes are consistent with a wind-driven divergence and upward Ekman pumping anomaly between 10° to 30°S and a wind-driven convergence and downward Ekman pumping anomaly to the north of 10°S (Fig. 4E). During the recovery of heat content and sea level in 2017–2018, temperature increased in the upper 1000 m south of 10°S with a maximum warming of up to 0.7°C between 100- and 300-m depth (Fig. 5, B and C), consistent with an anticyclonic wind anomaly and downward Ekman pumping in the subtropical SIO (Fig. 4F).

Temperature changes in 2014–2018 were associated with both the vertical and meridional displacements of isotherms (see contours in Fig. 5, A and B). The meridional Ekman transport anomalies appear to have had a minor impact on temperature changes in the upper 50 m. On the other hand, wind stress curl that drives Ekman

pumping affected the entire upper 1000-m water column by raising the isotherms in 2014–2016 and deepening them in 2016–2018. Furthermore, changes in wind stress curl and Ekman pumping are associated with changes in the meridional Sverdrup transport. More specifically, the upward Ekman pumping anomaly in the subtropical SIO in 2014–2016 translated to the southward Sverdrup transport anomaly in the entire water column, and vice versa for the downward Ekman pumping anomaly in 2016–2018. These are well reflected in the meridional shifts of isotherms between 10°S and 20°S, suggesting a contraction of the SIO subtropical gyre in 2016 and an expansion in 2018. Because the upper-ocean heat content at 20°S is greater than that at 10°S, these processes lead to cooling and warming of the SIO subtropical gyre between 10°S and 20°S, respectively.

Local versus remote (of Pacific origin) forcing

We have demonstrated so far that in 2014–2018, the local wind forcing had a considerable impact on the variability of the upper-ocean heat content and sea level in the SIO and altered the signals propagating from the eastern boundary. Signals at the eastern boundary are strongly linked to ENSO (Fig. 3, A and C) and, thus, are largely forced by processes in the equatorial western Pacific (33, 36, 38). In this section, using a linearized analytic 1.5-layer reduced-gravity model (see Materials and Methods), we quantify and analyze the combined and relative contributions of the eastern boundary forcing and the local wind stress curl to the interannual variability of the SIO heat content and sea level.

As illustrated in Fig. 6 (A and B), the 1.5-layer model simulates the observed SLA reasonably well. During 1995–2019, the model (the sum of the eastern boundary and local wind forcing) explains 50 to 70% and above 70% of the observed SLA variance in the WSIO and in the ESIO, respectively (dotted black curve in fig. S2). During 2010–2019, the portion of explained variance in the WSIO increases up to 90% (solid black curve in fig. S2). The eastern boundary forcing

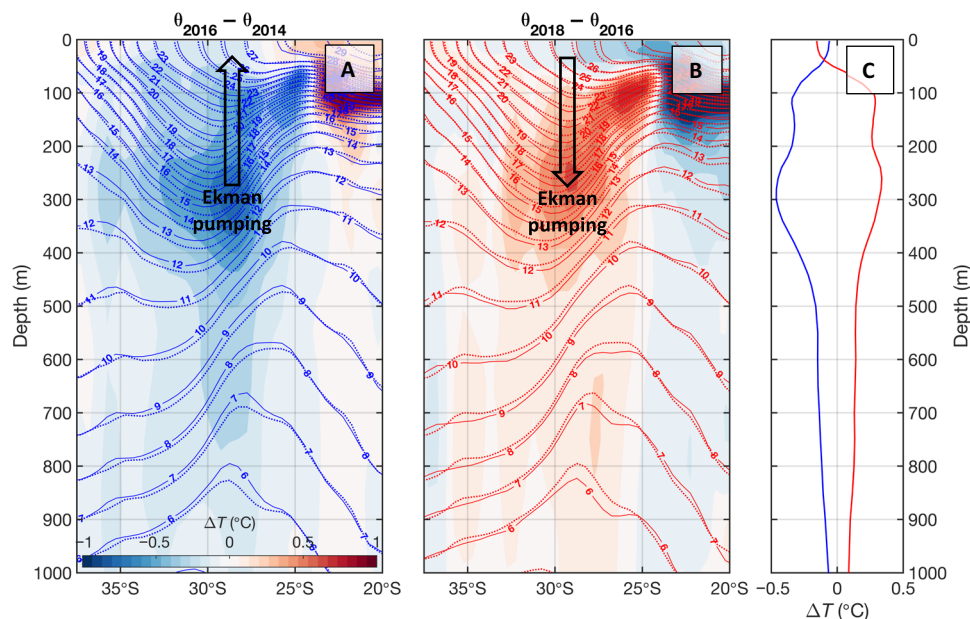


Fig. 5. Upper-ocean temperature changes. Profiles of the low-pass-filtered potential temperature, θ , averaged between 55°E and 110°E: (A) in 2016 (θ_{2016} ; blue contour), in 2014 (θ_{2014} ; dotted contour), and their difference, $\theta_{2016} - \theta_{2014}$ (color); (B) in 2018 (θ_{2018} ; red contour), in 2016 (θ_{2016} ; dotted contour), and their difference, $\theta_{2018} - \theta_{2016}$ (color); and (C) $\theta_{2016} - \theta_{2014}$ (blue line) and $\theta_{2018} - \theta_{2016}$ (red line) differences averaged between 55°E to 110°E and 10°S to 30°S.

alone (the first term on the right side of Eq. 4; Materials and Methods) exhibits slowly decaying Rossby waves (Fig. 6C). In general, the eastern boundary forcing adequately reproduces the signals that were able to propagate all the way from the eastern boundary to the western boundary, for example, the anomalies generated in 1997–2001 and in 2007–2009 (Fig. 6, A and C). As expected, the eastern boundary forcing, i.e., signals of the Pacific origin and strongly linked to ENSO variability (i.e., ocean tunnel effect), is dominant in the ESIO, where it explains most of the SLA variance to the east of 95°E (blue curves in fig. S2). The surface forcing from the local wind stress curl (the second term on the right side of Eq. 4; Materials and Methods) exhibits anomalies of similar amplitude that are generated in the SIO interior and also propagate westward as Rossby waves (Fig. 6D). The local wind forcing dominates in the WSIO. During 1995–2019, it explains only up to 40% of SLA variance, but in 2010–2019, this portion increases to 60 to 80% (red curves in fig. S2). It is remarkable how the relative contribution of the eastern boundary and local wind forcing breaks at the Ninety East Ridge (fig. S2), which serves as a natural barrier between the ESIO and WSIO, where remote and local forcing mechanisms dominate, respectively.

It is also interesting to note how the local wind stress curl modified the large positive SLAs that were observed at the eastern boundary in 1999–2002 and in 2010–2015 (Fig. 6C). These anomalies were partially compensated for by the two concurrent negative SLAs generated by the cyclonic wind anomalies but were still able to reach the western boundary (Fig. 6D). During these time periods, the eastern boundary anomalies and wind-driven anomalies in the WSIO were both associated with strong La Niña conditions. This example illustrates how the ENSO-driven atmospheric bridge and ocean tunnel effects interact with each other. On the contrary, the positive SLA in the WSIO in 2005–2008 was solely due to the local wind forcing, which suppressed the negative SLA signals radiated from the eastern boundary in 2003–2006.

Of particular interest for the objectives of this study are SLA changes during and after the 2014–2016 El Niño event (Fig. 6A). The ocean tunnel effect led to the reduction of SLA in the ESIO (Fig. 6C). At the same time, the ENSO-driven atmospheric bridge effect through the cyclonic wind anomaly (weaker trade winds) decreased SLA in the WSIO (Fig. 6D). While the negative SLA related to the ocean tunnel effect still prevailed in the ESIO in 2017–2019, the local wind forcing appears to be the main driver for SLA recovery

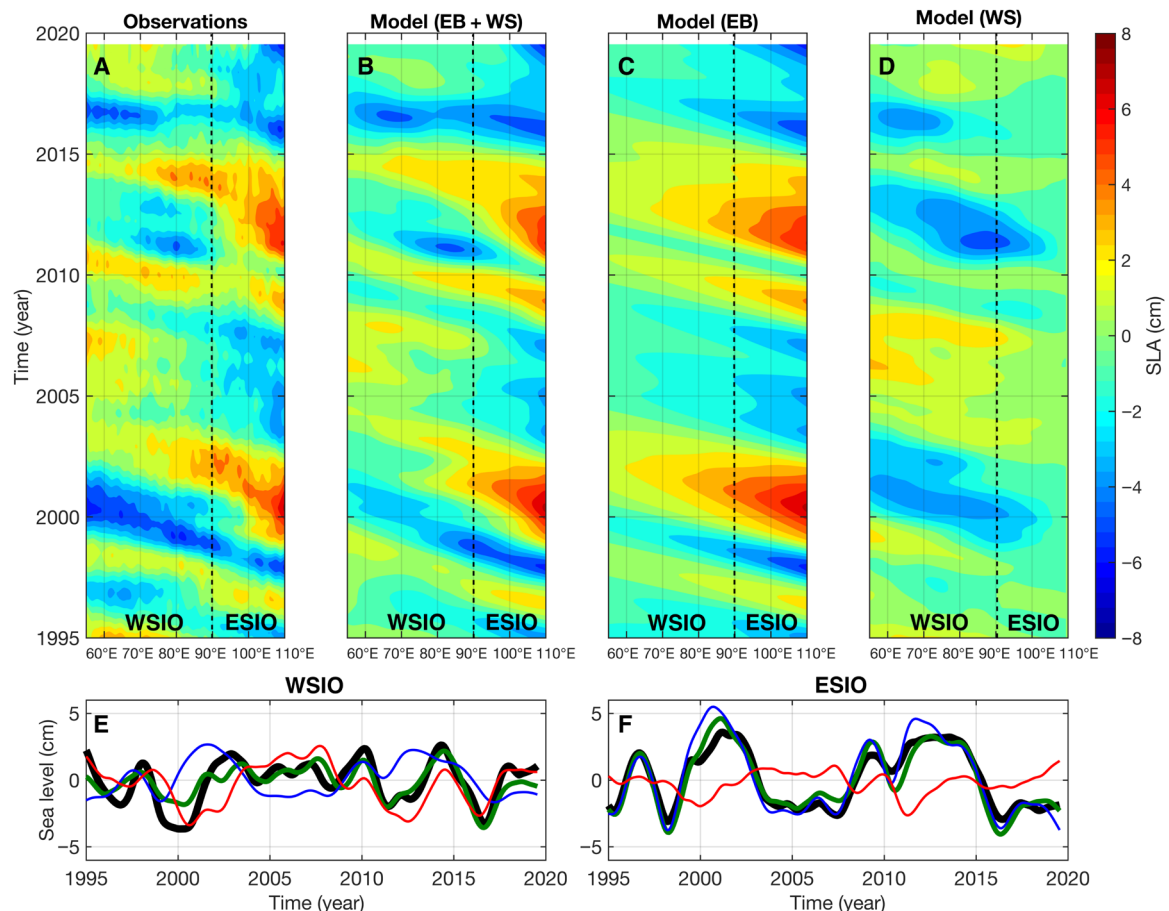


Fig. 6. Observed and modeled sea-level variability in the SIO. Hovmöller diagrams of (A) the observed, low-pass-filtered (with a cutoff period of 1 year), and detrended SLA averaged between 10°S and 30°S; (B) the modeled SLA using both the eastern boundary and the local wind stress curl forcing; (C) the modeled SLA obtained using the eastern boundary forcing (first term of Eq. 4) only, and (D) the modeled SLA obtained using the local wind stress curl forcing (second term of Eq. 4) only. (E and F) Time series of the observed SLA (black curves) and modeled SLA using the eastern boundary forcing (blue curves), the local wind stress curl forcing (red curves), and both forcing terms (green curves), averaged between (E) 55°E to 90°E and (F) 90°E to 110°E.

in the WSIO in 2017–2018 (Fig. 6D). This recovery was also related to the atmospheric bridge effect through the strengthening of trade winds during the weak 2017–2018 La Niña (Fig. 4F).

While the eastern boundary forcing does not explain significant variance in the WSIO, sea level signals related to the eastern boundary and the local wind forcing appear to have similar amplitudes and largely compensate for each other, reducing the WSIO sea level signals (Fig. 6E). However, the sea level decrease in 2014–2016 was contributed by both the local wind forcing (~60% of SLA change) and the eastern boundary forcing (~40% of SLA change). Thus, it is logical to conclude that the ocean tunnel and atmospheric bridge effects worked together to reduce heat content and sea level in the WSIO in 2014–2016, which nicely explains why the observed reduction was extremely strong and covered the entire SIO. The subsequent SLA recovery in 2017–2018 was primarily caused by the local wind forcing. In contrast to the WSIO, the SLA variability in the ESIO (Fig. 6F) was mostly driven by the eastern boundary forcing, strongly related to ENSO variability via the ocean tunnel effect. The impact of the local wind in the ESIO forcing was sizable, but of minor importance.

DISCUSSION

This paper addresses the evolution of the upper-ocean heat content and sea level in the SIO in 1993–2019. Although salinity changes make a sizable contribution, the observed interannual sea-level variability is mostly due to thermosteric changes, which makes sea level a good proxy for the upper-ocean heat content variability. Particular attention is given to changes associated with the most recent (and one of the strongest on record) 2014–2016 El Niño event, which led to an unprecedented (in observational record) cooling anomaly in the SIO, followed by a quick heat content recovery in 2017–2018 (Fig. 2A). In addition, we show why the basin-wide response of sea level and heat content in the subtropical SIO to the 1997–1998 El Niño was much smaller compared to the 2014–2016 El Niño.

The mechanisms responsible for the observed variability are studied in the context of westward-propagating Rossby waves. The associated sea level and, hence, heat content signals are radiated from the eastern boundary and/or generated by the local wind forcing over the basin's interior. The eastern boundary forcing signifies the remote ENSO forcing via the ocean tunnel effect, because signals at the eastern boundary largely originate in the Pacific and propagate into the SIO via the ITF and coastally trapped waves. The local wind forcing mostly refers to changes in trade and equatorial winds, related to ENSO via the atmospheric bridge effect and its interaction with IOD and other processes (e.g., SAM). While a detailed account of the relative importance of each mode of atmospheric variability is beyond the scope of this study, it appears that none of them alone is able to explain the whole complexity of the local wind forcing over the SIO.

One of the highlights of our findings is that the westward propagation from the eastern boundary cannot fully explain the observed basin-wide cooling that reached a maximum in both the WSIO and ESIO almost simultaneously in 2016. Furthermore, the 2014–2016 cooling in the WSIO ended abruptly with the 2017–2018 warming anomaly, while a cooling anomaly was still present in the ESIO (Figs. 2 and 3). A similar situation occurred earlier, when the 2003–2006 cooling anomaly near the eastern boundary did not propagate all the way to the western boundary but was interrupted over the Ninety

East Ridge by the local wind forcing in the WSIO during 2005–2008 (Fig. 3A). Nevertheless, most anomalies emanated from the eastern boundary were able to cross the SIO after some modification by local processes.

Local wind forcing that drives Ekman pumping anomalies in the SIO is found to be consistent with the observed reduction of sea level and heat content in 2014–2016 and their subsequent recovery in 2017–2018 (Fig. 4, E and F). A basin-wide cyclonic wind anomaly in 2014–2016 led to shoaling of isotherms in the upper-ocean and associated cooling, while anticyclonic wind anomalies in 2017–2018 led to deepening of isotherms and warming of the upper ocean. The associated temperature changes were mainly concentrated in the subsurface between 50 and 400 m with a magnitude of up to 1°C (Fig. 5).

We also note that compared with the 2014–2016 El Niño, there was no similar basin-wide cooling in the SIO during the strongest on record 1997–1998 El Niño (Fig. 2A). We show that this was partly related to westward propagation, i.e., the ocean tunnel effect. More specifically, when the El Niño-generated negative SLA was present in the ESIO in 1997–1998, the positive SLA generated during the 1995–1996 La Niña reached the WSIO (Fig. 3), thus resulting in a small net change of SLA in the subtropical SIO during 1996–1998 (Fig. 2A). In addition, the 1997–1998 El Niño occurred in-phase with a strong positive IOD (Fig. 2A and fig. S1A). Strong equatorial easterlies associated with the positive IOD favored the upper-ocean warming in the tropics and possibly inhibited the formation of the large-scale cyclonic wind anomaly in the subtropical SIO. In contrast, the easterly equatorial winds in 2014–2016 were much weaker than those in 1997–1998, mostly because they were suppressed by westerlies during the lowest on record negative IOD event in 2016 (Fig. 4, C and E).

Using a 1.5-layer reduced-gravity model under the long-wave approximation, we show that the interannual sea-level (and, hence, heat content) variability is dominated by the local wind forcing in the WSIO and by the eastern boundary forcing in the ESIO (Fig. 6). The El Niño-driven cooling in the ESIO in 2014–2016 was accompanied by the concurrent wind-driven cooling in the WSIO. The former process is attributed to the ocean tunnel effect, while the latter process represents the atmospheric bridge effect via the ENSO-modulated weakening of southeasterly trade winds over the SIO. The unprecedented basin-wide decrease of sea level and heat content in 2014–2016 occurred because of a rather unusual condition, during which the atmospheric bridge and ocean tunnel effects worked constructively, amplifying the impact of each other. The subsequent recovery in 2017–2018 was mainly driven by an anticyclonic wind anomaly formed over the SIO during the weak La Niña via the atmospheric bridge effect. As opposed to the unusual conditions during the 2014–2016 El Niño, the model reconstruction demonstrates that during the periods of strong La Niña in 1999–2001 and 2010–2014, the ocean tunnel and atmospheric bridge effects generated signals that partly compensated for each other. The La Niña-driven warming anomalies in 1999–2001 and 2010–2014 were substantially modified by the wind-driven cooling anomalies formed over the Ninety East Ridge as the southeasterly trade winds strengthened and shifted westward.

The results presented here highlight the complexity of the observed sea-level and heat content variability in the SIO, tightly linked to remote processes originating in the Pacific Ocean via the atmospheric bridge and ocean tunnel effects, as well as to local atmospheric and ocean dynamics. The decade-long heat accumulation

in the SIO in 2004–2013 may have preconditioned an unprecedented reduction of the ITF in 2014–2016 via reduced sea level difference between the western Pacific and Indian Oceans, possibly dampening the discharge of heat by the equatorial Pacific (44). In 2014–2016, the accumulated SIO heat may have released to the atmosphere to interfere with the regional seasonal climate cycle and/or produce a series of extreme weather events, while the remaining portion may have been sequestered to the deep ocean or transported to other parts of the ocean. As the SIO heat content has almost fully recovered after a remarkable drop in 2014–2016, it is possible that the pre-2014 SIO warming trend will continue in the near future. Further research using continued observations and ocean and climate models is required to investigate the far-reaching effects of the SIO heat content variability.

MATERIALS AND METHODS

In this study, we use observations of sea level and the upper-ocean thermohaline structure in combination with an atmospheric reanalysis. To focus on interannual time scales, the seasonal cycle is calculated by the least-squares fitting of the annual and semiannual harmonics and removed from all data fields and time series. The data are further low-pass filtered with a “Lowess” filter with a cutoff period of 1 year.

Sea level data

Large-scale changes of sea level on seasonal-to-interannual time scales are mostly steric, i.e., caused by changes in seawater density (45). Because density changes in low- and midlatitudes are mostly temperature driven (thermosteric), satellite observations of sea level in many places can be used as a proxy for oceanic heat content (46). Here, we use the monthly maps of SLA for the time period from January 1993 to July 2019 provided by Aviso (www.aviso.altimetry.fr). The global mean sea level rise has been subtracted to focus on dynamic sea-level variability. The mean dynamic topography shown in Fig. 1 depicts the mean surface geostrophic circulation in the Indian Ocean.

Argo data

To study changes in the upper-ocean (0 to 2000 m) thermohaline structure, we use the monthly gridded profiles of temperature (T) and salinity (S) measured by Argo floats since 2004 and provided by the Scripps Institution of Oceanography (47). The profiles are used to calculate the steric sea level (SSL) anomalies relative to 2000-m depth, which can be approximately (ignoring the nonlinearity terms in the equation of state) decomposed into the thermosteric sea level (TSL) and halosteric sea level (HSL) contributions to SLA (Figs. 2, and 4, B and C)

$$\text{SSL} \approx \text{TSL} + \text{HSL} = -\frac{1}{g} \left[\int_{2000}^0 \delta_T dp + \int_{2000}^0 \delta_S dp \right] \quad (1)$$

where $\delta_T = \alpha(\bar{S}, T, p) - \alpha(35, 0, p)$ and $\delta_S = \alpha(S, \bar{T}, p) - \alpha(35, 0, p)$ are the thermosteric and halosteric specific volume (α) anomalies, respectively, g is the gravity, p is the pressure, and the overbar indicates the time-mean values. The obtained thermosteric SLAs are proportional to the upper 2000-m heat content anomalies.

Atmospheric data

To link the observed changes in sea level and heat content to wind forcing, we use the 10-m wind velocity and surface wind stress data

in 1979–2019 provided by the ECMWF's (European Centre for Medium-Range Weather Forecasts) ERA-Interim reanalysis (www.ecmwf.int) (48). Wind stress is used to compute Ekman pumping anomaly (W_E ; positive upward) relative to January 1979–December 2018 climatology

$$W_E = \nabla \times \frac{\boldsymbol{\tau}'}{\rho f} \quad (2)$$

where $\boldsymbol{\tau}' = \boldsymbol{\tau} - \bar{\boldsymbol{\tau}}$, $\boldsymbol{\tau}$ is the wind stress vector, and the overbar indicates the 1979–2018 average wind stress.

Climate indices

To represent the atmospheric and oceanic anomalies that occur during ENSO events, we use the MEI provided by the National Oceanic and Atmospheric Administration (NOAA) Earth System Research Laboratory's Physical Sciences Division (www.esrl.noaa.gov/psd). MEI is based on five variables from the tropical Pacific: sea-level pressure, zonal and meridional components of the surface wind, sea surface temperature, and outgoing longwave radiation (49). Positive (negative) MEI refers to El Niño (La Niña) conditions.

A local ocean-atmosphere phenomenon in the Indian Ocean coupled to ENSO is known as the IOD. The IOD index is determined by sea surface temperature differences between the western equatorial Indian Ocean (50°E to 70°E and 10°S to 10°N) and the southeastern equatorial Indian Ocean (90°E to 110°E and 10°S to 0°). The positive (negative) IOD means that the surface of western Indian Ocean is warmer (cooler) than the surface of the eastern Indian Ocean. We use the IOD index provided by the Japan Agency for Marine-Earth Science and Technology (JAMSTEC; www.jamstec.go.jp/aplinfo/sintexf/e/iod/about_iod.html).

Model for sea-level variability

The large-scale variability of sea level and heat content away from the equator is strongly influenced by Rossby waves. In the SIO, either Rossby waves emanate from the eastern boundary, where their generation is modulated by signals coming from the Pacific, or they are generated by local wind forcing. To quantify the relative impact of these processes to the observed sea level changes, we use a linear 1.5-layer reduced-gravity model under the long-wave approximation (38, 50). The long-wave linear vorticity equation governing the baroclinic component of SLA, η , can be expressed as follows

$$\frac{\partial \eta}{\partial t} = c_R \frac{\partial \eta}{\partial x} - \frac{g' \nabla \times \boldsymbol{\tau}'}{\rho_0 g f} - \varepsilon \eta \quad (3)$$

where c_R is the zonal phase speed of long baroclinic Rossby waves, g is the gravity, g' is the reduced gravity, and ε is a frictional damping coefficient added to dissipate propagating signal with time. The integration of Eq. 4 along the baroclinic Rossby wave characteristic yields the following solution in the longitude-time (x - t) plane (38, 50)

$$\eta(x, t) = \eta \left(x_e, t - \frac{x - x_e}{c_R} \right) e^{-\varepsilon \left(\frac{x - x_e}{c_R} \right)} - \frac{g'}{\rho_0 g f c_R} \int_{x_e}^x \nabla \times \boldsymbol{\tau}' \left(x', t - \frac{x - x'}{c_R} \right) e^{-\varepsilon \left(\frac{x - x'}{c_R} \right)} dx' \quad (4)$$

where x_e is the longitude of the eastern boundary. The first term on the right side of Eq. 4 is the sea level signal that originates at the eastern boundary, while the second term is the sea level signal

generated by the local wind stress curl. Both signals propagate westward as Rossby waves. The model is initialized with the low-pass-filtered altimetry SLA at 110°E , (x_e, t) . The reduced gravity is estimated as $g' = c_g^2/H_t$, where $c_g \approx 3 \text{ m s}^{-1}$ is the baroclinic gravity-wave phase speed from Chelton *et al.* (51) and $H_t \approx 150 \text{ m}$ is the thermocline depth (estimated as the depth of the 20°C isotherm in Argo data) characteristic for the SIO between 10°S to 30°S . This yields $g' \approx 0.06 \text{ m s}^{-2}$. On the basis of the Hovmöller diagram of SLA in the SIO (Fig. 4A), we set $c_R = 0.1 \text{ m s}^{-1}$. The best fit of the reconstructed SLA to observations is achieved with the dissipation coefficient $\varepsilon = (1.3 \text{ year})^{-1}$.

Statistical analysis

Linear regression is used to relate the atmospheric circulation patterns to ENSO and IOD: The ERA-Interim winds and derived Ekman pumping anomalies are projected on standardized (divided by SD) MEI and IOD index, respectively. The obtained regression coefficients are in meter per second per SD for wind velocities and meter per month per SD for Ekman pumping (Fig. 4, A and B).

The 95% significance level for correlations between the Ekman pumping anomalies and MEI/IOD (fig. S1B) is estimated using Monte Carlo simulations as follows. First, the number of degrees of freedom for each time series (i) in a pair is estimated as $N_i^* = L/T_i^*$, where $L = \Delta t N$ is the length of the time series for N lag steps, Δt , and T_i^* is the integral time scale (52). Second, 10,000 pairs of random time series of the length N_i^* were generated and subsampled to make their length the same with the original time series. Last, the 95% significance level is given by the 95th percentile of correlations between the pairs of simulated time series.

The relative contribution of eastern boundary and local wind stress forcing terms is estimated by computing the explained variance (fig. S2). The fraction of variance (F) of a variable x , explained by another variable y , is computed as $F = 100\% \times \left[1 - \frac{\text{var}(x - y)}{\text{var}(x)}\right]$.

SUPPLEMENTARY MATERIALS

Supplementary material for this article is available at <http://advances.sciencemag.org/cgi/content/full/6/36/eabc1151/DC1>

REFERENCES AND NOTES

- M. Rhein, S. R. Rintoul, S. Aoki, E. Campos, D. Chambers, R. A. Feely, S. Gulev, G. C. Johnson, S. A. Josey, A. Kostianoy, C. Mauritzen, D. Roemmich, L. D. Talley, F. Wang, Observations: Ocean, in *Climate Change 2013: The Physical Science Basis. Contribution of Working Group I to the Fifth Assessment Report of the Intergovernmental Panel on Climate Change*, T. F. Stocker, D. Qin, G.-K. Plattner, M. Tignor, S. K. Allen, J. Boschung, A. Nauels, Y. Xia, V. Bex, P. M. Midgley, Eds. (Cambridge Univ. Press, 2013).
- M. Llovel, L. Terray, Observed southern upper-ocean warming over 2005–2014 and associated mechanisms. *Environ. Res. Lett.* **11**, 124023 (2016).
- D. L. Volkov, S.-K. Lee, F. W. Landerer, R. Lumpkin, Decade-long deep-ocean warming detected in the subtropical South Pacific. *Geophys. Res. Lett.* **44**, 927–936 (2017).
- Y. Zhang, M. Feng, Y. Du, H. E. Phillips, N. L. Bindoff, M. J. McPhaden, Strengthened Indonesian Throughflow drives decadal warming in the South Indian Ocean. *Geophys. Res. Lett.* **45**, 6167–6175 (2018).
- S.-K. Lee, W. Park, M. O. Baringer, A. L. Gordon, B. Huber, Y. Liu, Pacific origin of the abrupt increase in Indian Ocean heat content during the warming hiatus. *Nat. Geosci.* **8**, 445–449 (2015).
- J. Jyoti, P. Swapna, R. Krishnan, C. V. Naidu, Pacific modulation of accelerated south Indian Ocean sea level rise during the early 21st Century. *Climate Dynam.* **53**, 4413–4432 (2019).
- M. M. Ali, D. Swain, T. Kashyap, J. P. McCreary, P. V. Nagamani, Relationship between cyclone intensities and sea surface temperature in the tropical Indian Ocean. *IEEE Geosci. Remote Sens. Lett.* **10**, 841–844 (2013).
- T. Venugopal, M. M. Ali, M. A. Bourassa, Y. Zheng, G. J. Goni, G. R. Foltz, M. Rajeevan, Statistical evidence for the role of southwestern Indian Ocean heat content in the Indian Summer Monsoon Rainfall. *Sci. Rep.* **8**, 12092 (2018).
- E. C. J. Oliver, M. G. Donat, M. T. Burrows, P. J. Moore, D. A. Smale, L. V. Alexander, J. A. Benthuyzen, M. Feng, A. S. Gupta, A. J. Hobday, N. J. Holbrook, S. E. Perkins-Kirkpatrick, H. A. Scannell, S. C. Straub, T. Wernberg, Longer and more frequent marine heatwaves over the past century. *Nat. Commun.* **9**, 1324 (2018).
- J. Zinke, A. Hoell, J. M. Lough, M. Feng, A. J. Kuret, H. Clarke, V. Ricca, K. Rankenburg, M. T. M. Culloch, Coral record of southeast Indian Ocean marine heatwaves with intensified Western Pacific temperature gradient. *Nat. Commun.* **6**, 8562 (2015).
- F. A. Schott, S.-P. Xie, J. P. McCreary Jr., Indian Ocean circulation and climate variability. *Rev. Geophys.* **47**, RG1002 (2009).
- A. L. Gordon, A. Napitu, B. A. Huber, L. K. Gruenbourg, K. Pujiana, T. Agustiadhi, A. Kuswardani, N. Mbay, A. Setiawan, Makassar Strait throughflow seasonal and interannual variability: An overview. *J. Geophys. Res. Oceans* **124**, 3724–3736 (2019).
- W. Cai, P. van Renssch, T. Cowan, H. H. Hendon, An asymmetry in the IOD and ENSO teleconnection pathway and its impact on Australian climate. *J. Climate* **25**, 6318–6329 (2012).
- S. Chakravorty, C. Gnanaseelan, J. S. Chowdary, J.-J. Luo, Relative role of El Niño and IOD forcing on the southern tropical Indian Ocean Rossby waves. *J. Geophys. Res. Oceans* **119**, 5105–5122 (2014).
- M. F. Stuecker, A. Timmermann, F.-F. Jin, Y. Chikamoto, W. Zhang, A. T. Wittenberg, E. Widiasih, S. Zhao, Revisiting ENSO/Indian Ocean Dipole phase relationships. *Geophys. Res. Lett.* **44**, 2481–2492 (2017).
- J. Sprintall, S. E. Wijffels, R. Molcard, I. Jaya, Direct estimates of the Indonesian Throughflow entering the Indian Ocean: 2004–2006. *J. Geophys. Res.* **114**, C07001 (2009).
- A. L. Gordon, Inter-ocean exchange of thermocline water. *J. Geophys. Res.* **91**, 5037–5046 (1986).
- A. L. Gordon, R. A. Fine, Pathways of water between the Pacific and Indian Oceans in the Indonesian Seas. *Nature* **379**, 146–149 (1996).
- K. Vranes, A. L. Gordon, A. Ffield, The heat transport of the Indonesian Throughflow and implications for the Indian Ocean heat budget. *Deep Sea Res. Pt. II* **49**, 1391–1410 (2002).
- A. L. Gordon, J. Sprintall, H. M. Van Aken, D. Susanto, S. Wijffels, R. Molcard, A. Ffield, W. Pranowo, S. Wirasantosa, The Indonesian Throughflow during 2004–2006 as observed by the INSTANT program. *Dynam. Atmos. Ocean* **50**, 115–128 (2010).
- A. L. Gordon, Indian-Atlantic transfer of thermocline water at the Agulhas Retroflection. *Science* **227**, 1030–1033 (1985).
- J. R. E. Lutjeharms, J. Cooper, Interbasin leakage through Agulhas Current filaments. *Deep Sea Res. Pt. I* **43**, 213–238 (1996).
- J. V. Durgadoo, S. Rühs, A. Biastoch, C. W. B. Böning, Indian Ocean sources of Agulhas leakage. *J. Geophys. Res. Oceans* **122**, 3481–3499 (2017).
- Q. Song, A. L. Gordon, M. Visbeck, Spreading of the Indonesian Throughflow in the Indian Ocean. *J. Phys. Oceanogr.* **34**, 772–792 (2004).
- R. O. R. Y. Thompson, Observations of the Leeuwin Current off Western Australia. *J. Phys. Oceanogr.* **14**, 623–628 (1984).
- G. Meyers, Variation of Indonesian Throughflow and the El Niño–Southern Oscillation. *J. Geophys. Res.* **101**, 255–12,263 (1996).
- Y. Masumoto, Effects of interannual variability in the eastern Indian Ocean on the Indonesian Throughflow. *J. Oceanogr.* **58**, 175–182 (2002).
- M. H. England, F. Huang, On the interannual variability of the Indonesian Throughflow and its linkage with ENSO. *J. Climate* **18**, 1435–1444 (2005).
- D. Tillinger, A. L. Gordon, Fifty years of the Indonesian Throughflow. *J. Climate* **22**, 6342–6355 (2009).
- J. Sprintall, A. Révelard, The Indonesian Throughflow response to Indo-Pacific climate variability. *J. Geophys. Res. Oceans* **119**, 1161–1175 (2014).
- M. Li, A. L. Gordon, J. Wei, L. K. Gruenbourg, G. Jiang, Multi-decadal timeseries of the Indonesian Throughflow. *Dynam. Atmos. Ocean* **81**, 84–95 (2018).
- M. Feng, N. Zhang, Q. Liu, S. Wijffels, The Indonesian Throughflow, its variability and centennial change. *Geosci. Lett.* **5**, 3 (2018).
- K. Pujiana, M. J. McPhaden, A. L. Gordon, A. M. Napitu, Unprecedented response of Indonesian Throughflow to anomalous Indo-Pacific climatic forcing in 2016. *J. Geophys. Res. Oceans* **124**, 3737–3754 (2019).
- M. Feng, Y. Li, G. Meyers, Multidecadal variations of Fremantle sea level: Footprint of climate variability in the tropical Pacific. *Geophys. Res. Lett.* **31**, L16302 (2004).
- K. Pujiana, A. L. Gordon, J. Sprintall, Intraseasonal Kelvin wave in Makassar Strait. *J. Geophys. Res. Oceans* **118**, 2023–2034 (2013).
- L. L. Trenary, W. Han, Intraseasonal-to-interannual variability of South Indian Ocean sea level and thermocline: Remote versus local forcing. *J. Phys. Oceanogr.* **42**, 602–627 (2012).
- J. T. Poterma, Contribution of equatorial Pacific winds to southern tropical Indian Ocean Rossby waves. *J. Geophys. Res.* **106**, 2407–2422 (2001).
- W. Zhuang, M. Feng, Y. Du, A. Schiller, D. Wang, Low-frequency sea level variability in the southern Indian Ocean and its impacts on the oceanic meridional transports. *J. Geophys. Res. Oceans* **118**, 1302–1315 (2013).

39. S. Zheng, M. Feng, Y. Du, X. Meng, W. Yu, Interannual variability of eddy kinetic energy in the subtropical Southeast Indian Ocean associated with the El Niño–Southern Oscillation. *J. Geophys. Res. Oceans* **123**, 1048–1061 (2018).
40. Y. Masumoto, G. Meyers, Forced Rossby waves in the southern tropical Indian Ocean. *J. Geophys. Res. Oceans* **103**, 27589–27602 (1998).
41. F. Birol, R. Morrow, Source of the baroclinic waves in the southeast Indian Ocean. *J. Geophys. Res. Oceans* **106**, 9145–9160 (2001).
42. L. K. Gruenburg, A. L. Gordon, Variability in Makassar Strait heat flux and its effect on the eastern tropical Indian Ocean. *Oceanography* **31**, 80–87 (2018).
43. B. Lu, H.-L. Ren, A. A. Scaife, J. Wu, N. Dunstone, D. Smith, J. Wan, R. Eade, C. M. Lachlan, M. Gordon, An extreme negative Indian Ocean Dipole event in 2016: Dynamics and predictability. *Climate Dynam.* **51**, 89–100 (2018).
44. M. Mayer, M. A. Balmaseda, L. Haimberger, Unprecedented 2015/2016 Indo-Pacific heat transfer speeds up tropical Pacific heat recharge. *Geophys. Res. Lett.* **45**, 3274–3284 (2018).
45. A. E. Gill, P. P. Niller, The theory of the seasonal variability in the ocean. *Deep Sea Res.* **20**, 141–178 (1973).
46. D. P. Chambers, B. D. Tapley, R. H. Stewart, Measuring heat storage changes in the equatorial Pacific: A comparison between TOPEX altimetry and Tropical Atmosphere–Ocean buoys. *J. Geophys. Res.* **103**, 18591–18597 (1998).
47. D. Roemmich, J. Gilson, The 2004–2008 mean and annual cycle of temperature, salinity, and steric height in the global ocean from the Argo Program. *Oceanography* **82**, 81–100 (2009).
48. D. P. Dee, S. M. Uppala, A. J. Simmons, P. Berrisford, P. Poli, S. Kobayashi, U. Andrae, M. A. Balmaseda, G. Balsamo, P. Bauer, P. Bechtold, A. C. M. Beljaars, L. van de Berg, J. Bidlot, N. Bormann, C. Delsol, R. Dragani, M. Fuentes, A. J. Geer, L. Haimberger, S. B. Healy, H. Hersbach, E. V. Hólm, L. Isaksen, P. Kållberg, M. Köhler, M. Matricardi, A. P. McNally, B. M. Monge-Sanz, J.-J. Morcrette, B.-K. Park, C. Peubey, P. de Rosnay, C. Tavalato, J.-N. Thépaut, F. Vitart, The ERA-Interim reanalysis: Configuration and performance of the data assimilation system. *Quart. J. Roy. Meteor. Soc.* **137**, 553–597 (2011).
49. K. Wolter, M. S. Timlin, El Niño/Southern Oscillation behaviour since 1871 as diagnosed in an extended multivariate ENSO index (MEI.ext). *Int. J. Climatol.* **31**, 1074–1087 (2011).
50. B. Qiu, Large-scale variability in the midlatitude subtropical and subpolar North Pacific Ocean: Observations and causes. *J. Phys. Oceanogr.* **32**, 353–375 (2002).
51. D. B. Chelton, R. A. deSzoeke, M. G. Schlax, K. E. Naggar, N. Siwertz, Geographical variability of the First Baroclinic Rossby radius of deformation. *J. Phys. Oceanogr.* **28**, 433–460 (1998).
52. R. E. Thomson, W. J. Emery, *Data Analysis Methods in Physical Oceanography* (Elsevier B.V., ed. 3, 2014).

Acknowledgments

Funding: This work was supported by the NASA Ocean Surface Topography Science Team program (via the grant NNX17AH59G) and by the NOAA Atlantic Oceanographic and Meteorological Laboratory, and it was carried out, in part, under the auspices of the Cooperative Institute of Marine and Atmospheric Studies (CIMAS), a Cooperative Institute of the University of Miami and NOAA (cooperative agreement NA10OAR4320143). A.L.G.'s support was derived from the Office of Naval Research grant N00014-17-1-2394.

Lamont-Doherty Earth Observatory contribution number 8430. **Author contributions:**

D.L.V. conceived this study with contributions from S.-K.L. D.L.V. supervised the project, performed the data analysis, coded the reduced gravity model, produced the figures, and wrote the manuscript. S.-K.L., A.L.G., and M.R. assisted in interpretation of the results. All authors made suggestions and approved the final manuscript. **Competing interests:** The authors declare that they have no competing interests. **Data and materials availability:**

The altimeter products were produced and distributed by Aviso+ (www.aviso.altimetry.fr/), as part of the Ssalto ground processing segment. The Argo data were collected and made freely available by the International Argo Program and the national programs that contribute to it (www.argo.ucsd.edu). The Argo Program is part of the Global Ocean Observing System. The ERA-Interim reanalysis is produced and distributed by the ECMWF (www.ecmwf.int). The MEI is provided by the NOAA Earth System Research Laboratory's Physical Sciences Division (www.esrl.noaa.gov/psd/). The IOD index is provided by the Japan Agency for Marine–Earth Science and Technology (www.jamstec.go.jp/aplinfo/sintexf/e/iod/about_iod.html). All data needed to evaluate the conclusions in the paper are present in the paper and/or the Supplementary Materials. Additional data related to this paper may be requested from the authors.

Submitted 7 April 2020

Accepted 21 July 2020

Published 4 September 2020

10.1126/sciadv.abc1151

Citation: D. L. Volkov, S.-K. Lee, A. L. Gordon, M. Rudko, Unprecedented reduction and quick recovery of the South Indian Ocean heat content and sea level in 2014–2018. *Sci. Adv.* **6**, eabc1151 (2020).

Unprecedented reduction and quick recovery of the South Indian Ocean heat content and sea level in 2014–2018

Denis L. Volkov, Sang-Ki Lee, Arnold L. Gordon and Michael Rudko

Sci Adv 6 (36), eabc1151.
DOI: 10.1126/sciadv.abc1151

ARTICLE TOOLS

<http://advances.sciencemag.org/content/6/36/eabc1151>

SUPPLEMENTARY MATERIALS

<http://advances.sciencemag.org/content/suppl/2020/08/31/6.36.eabc1151.DC1>

REFERENCES

This article cites 50 articles, 1 of which you can access for free
<http://advances.sciencemag.org/content/6/36/eabc1151#BIBL>

PERMISSIONS

<http://www.sciencemag.org/help/reprints-and-permissions>

Use of this article is subject to the [Terms of Service](#)

Science Advances (ISSN 2375-2548) is published by the American Association for the Advancement of Science, 1200 New York Avenue NW, Washington, DC 20005. The title *Science Advances* is a registered trademark of AAAS.

Copyright © 2020 The Authors, some rights reserved; exclusive licensee American Association for the Advancement of Science. No claim to original U.S. Government Works. Distributed under a Creative Commons Attribution NonCommercial License 4.0 (CC BY-NC).